Carbon speciation in organic fossils using 2D to 3D x-ray Raman multispectral imaging

Rafaella Georgiou, Pierre Gueriau, Christoph Sahle, Sylvain Bernard, Alessandro Mirone, Romain Garrouste, Uwe Bergmann, Jean-Pascal Rueff, Loïc Bertrand

APPLIED SCIENCES AND ENGINEERING

Carbon speciation in organic fossils using 2D to 3D x-ray Raman multispectral imaging

Rafaella Georgiou[1,2], Pierre Gueriau[1,3], Christoph J. Sahle[4], Sylvain Bernard[5], Alessandro Mirone[4], Romain Garrouste[6], Uwe Bergmann[7]*, Jean-Pascal Rueff[2,8]*, Loïc Bertrand[1,2]*

The in situ two-dimensional (2D) and 3D imaging of the chemical speciation of organic fossils is an unsolved problem in paleontology and cultural heritage. Here, we use x-ray Raman scattering (XRS)–based imaging at the carbon K-edge to form 2D and 3D images of the carbon chemistry in two exceptionally preserved specimens, a fossil plant dating back from the Carboniferous and an ancient insect entrapped in 53-million-year-old amber. The 2D XRS imaging of the plant fossil reveals a homogeneous chemical composition with micrometric "pockets" of preservation, likely inherited from its geological history. The 3D XRS imaging of the insect cuticle displays an exceptionally well preserved remaining chemical signature typical of polysaccharides such as chitin around a largely hollowed-out inclusion. Our results open up new perspectives for in situ chemical speciation imaging of fossilized organic materials, with the potential to enhance our understanding of organic specimens and their paleobiology.

INTRODUCTION

The chemistry of ancient organic materials carries information of their original nature. Because this information is difficult to decode and limited by degradation, the depiction of chemical signatures preserved in the fossil record constitutes one of the essential challenges for paleontologists.

In some rare cases, organic structures can be preserved in rocks. Emblematic cases of organic preservation include mammoths entombed in the permafrost (*1*, *2*), insects trapped in amber (*3*–*6*), colored dinosaur feathers (*7*), and charcolified or lignitic fossil plants from the Carboniferous used as the main source for coal. Although fascinating, the search for ancient biomolecules imposes stringent interpretational and analytical challenges as (i) taphonomic and diagenetic processes may strongly affect original chemistry, (ii) contaminants are likely present at the surface of the samples, and (iii) carbon-based compounds can be preserved as traces.

Most fossil biogenic organic compounds have been detected in their native form using invasive analysis such as gas chromatography/mass spectrometry [GC/MS; e.g., (*8*, *9*)] or amplified by polymerase chain reaction [e.g., (*1*, *2*, *4*)]. However, these measurements are performed on extracts and therefore only represent averaged information over the sampling volume and do not yield the spatial complexity of the chemistry of these specimens for which imaging is a requisite. The development of new analytical tools and/or technical improvements toward higher sensitivity or resolution have recently pushed forward the search for traces of ancient biomolecules in the fossil record (*10*).

For instance, fourier transform infrared (FTIR) mapping revealed the preservation of amide and thiol groups of the β-keratin molecule in ca. 50-million-year-old reptile skin from Utah, USA (*11*). Time-of-flight secondary ion mass spectrometry (ToF-SIMS) data provided identification of hemoglobin-derived porphyrin molecules in a ca. 46-million-year-old blood-engorged mosquito from Montana, USA (*12*). In conjunction with immunohistochemical staining and FTIR imaging, ToF-SIMS identified endogenous proteinaceous and lipid constituents, keratinocytes, and branched melanophores, which give evidence for homeothermy and crypsis in a ca. 180-million-year-old ichthyosaur from Germany (*13*). One of the most promising experimental approaches is scanning transmission x-ray microscopy (STXM), a synchrotron-based soft x-ray technique that can probe speciation of light elements in micrometric samples at a spatial resolution of a few tens of nanometers (*14*). Carbon K-edge spectra obtained on carbonaceous systems consist of spectral features that can differentiate organic compounds (*15*). Applied to paleontology, STXM identified partially degraded sporopollenin molecules within a ca. 230-million-year-old lycophyte megaspore from France (*16*) and partially preserved chitin-protein complexes within the cuticles of a ca. 310-million-year-old scorpion from Illinois, USA, and of a ca. 420-million-year-old eurypterid from Canada (*17*). This technique even allowed documenting the chemical nature of ancient (several billion years old) organic microfossils (*18*).

However, these techniques present some limitations, the main one being the lack of bulk sensitivity. STXM-based x-ray absorption near-edge structure (XANES) spectroscopy only allows probing thin samples (i.e., samples transparent to x-rays at the transition energy of the element of interest). FTIR, Raman, and ToF-SIMS imaging also only provide surface sensitivity. Thus, any contamination of the surface by exogenous organic matter, and sample roughness as well, can compromise data acquisition and interpretation. This "black and white" situation where organic compounds absorb either too much or too little (hard x-rays) to allow meaningful imaging, depending on the nature of the probe, still poses numerous challenges to the depiction of the three-dimensional (3D) chemical speciation of primarily organic systems. A method providing spatially resolved

[1]IPANEMA, CNRS, ministère de la culture, Université de Versailles Saint-Quentin-en-Yvelines, Université Paris-Saclay, BP 48 St. Aubin, 91192 Gif-sur-Yvette, France. [2]Synchrotron SOLEIL, l'Orme des Merisiers, BP 48 St. Aubin, 91192 Gif-sur-Yvette, France. [3]Institute of Earth Sciences, University of Lausanne, Géopolis, CH-1015 Lausanne, Switzerland. [4]ESRF–The European Synchrotron, 71, avenue des Martyrs, CS 40220, 38043 Grenoble, France. [5]Muséum National d'Histoire Naturelle, Sorbonne Université, UMR CNRS 7590, IRD, Institut de Minéralogie, de Physique des Matériaux et de Cosmochimie (IMPMC), 75005 Paris, France. [6]Institut de Systématique Evolution Biodiversité (ISYEB), UMR 7205 MNHN/CNRS/Sorbonne Univ./EPHE/Univ. Antilles, Muséum National d'Histoire Naturelle, 57 rue Cuvier, CP 50, F-75005 Paris, France. [7]Stanford PULSE Institute, SLAC National Accelerator Laboratory, Menlo Park, CA, USA. [8]Sorbonne Université, CNRS, Laboratoire de Chimie Physique–Matière et Rayonnement, LCPMR, F-75005 Paris, France.
*Corresponding author. Email: loic.bertrand@synchrotron-soleil.fr (L.B.); jean-pascal.rueff@synchrotron-soleil.fr (J.-P.R.); bergmann@slac.stanford.edu (U.B.)

information of organic carbon speciation in 3D and over large areas appears critically required to overcome these limitations.

Here, we report the unprecedented use of a hard x-ray probe for the element-specific chemical bulk imaging of ancient materials. Taking advantage of the capability of nonresonant x-ray Raman scattering (XRS) for direct tomography with chemical bond contrast (*19*), we develop 2D and 3D XRS spectral imaging for cultural heritage and geosciences. The large penetrative power of hard x-rays enables the measurement to be done in a noninvasive way, with no particular preparation nor specific experimental conditions, in air, and provides information that is not compromised by surface contamination by ensuring that the dominant signal contribution is from the bulk of the probed material (*20*). XRS 2D and 3D imaging are demonstrated against a fragment of *Lepidodendron* trunk from the Upper Carboniferous [ca. 305 million years (Ma) old] of Pas-de-Calais (France) and an Eocene ant (ca. 53 Ma old) entrapped in amber from Oise (France), respectively. The present results reveal local "pockets" of preservation in the chemical composition of the plant fossil, likely inherited from its geological history, while they acquaint the exceptional preservation of the insect cuticle by showing chemical signatures of polysaccharides such as chitin.

RESULTS AND DISCUSSION

We collected XRS carbon K-edge intensities using mapping (or raster scanning) by sequentially moving objects across the photon beam at a given incident energy while measuring the scattered intensity. Several of these maps are acquired at different energy losses through the carbon K-edge to produce a hyperspectral data cube.

Illuminating a sample with an incident energy E and setting a fixed analyzer energy E_f, the energy loss $\Delta E = E - E_f$ can create electronic excitations. If ΔE is tuned to a transition involving a bound electron, then the resulting spectroscopy is called XRS spectroscopy. Beside a q-dependent background that is dominated by Compton scattering and collective valence electron excitations such as plasmons at high and low momentum transfers (q), respectively, the XRS spectrum generally contains nondispersive features that are generated when a fraction of incident photon energy is transferred to the sample inner shell electrons, promoting them into unoccupied states (*21*). XRS therefore enables the measurement of the near-edge excitation spectrum in the energy loss domain. It combines the chemical sensitivity of x-ray absorption spectroscopy (XAS) for the study of the speciation of light elements such as carbon with the benefit of high photon energy (range, 6 to 13 keV), discarding the substantial experimental constraints of XAS at the low energy of the carbon K-edge (range, 280 to 350 eV). XRS has demonstrated a great potential to probe carbon speciation in homogeneous liquid and solid carbon–based samples that are poor in heavier elements (absorption of x-ray from the latter represents the main limitation of this technique). XRS has been shown to be a promising means to identify the chemical speciation of light elements in a range of systems from oil cuts to artists' pigments (*20*–*22*). The proof of concept of imaging has been established on a model object (*19*), yet XRS imaging (XRI) of real-life materials has never been studied.

Microscale 2D imaging of carbon on centimetric Carboniferous plants

We used XRI to study a fragment of *Lepidodendron* trunk collected on an Upper Carboniferous (ca. 305 Ma old) coal slag heap in Noyelles-lez-Lens, France (Fig. 1, A to C). The fossil fragment, easily recognizable by its characteristic diamond-shaped pattern, is ca. 6 cm long and 2.5 cm wide and lies on a black shale, yellowish in places, which also includes other plant fragments. Most of the *Lepidodendron* trunk has the same appearance and color as the shale, but it also contains a thicker, vitreous black to very shiny material (extremely similar to vitrinite) distributed along the edges of most diamond-shaped leaf scars. A few beige patches are irregularly distributed over the fossil.

XRI produces carbon maps with a micrometric spatial resolution (down to a few micrometers as defined by the beam size) over large pluricentimetric objects. In contrast to carbon mapping using scanning electron microscopy with energy-dispersive x-ray spectroscopy, 2D XRI provides bulk mapping such that the carbon signal is not (or minimally) hampered by contamination or surface roughness. Collecting a map before and after the K-edge allows reconstructing an edge jump map, a map of carbon concentration within the sample. The map obtained appears unexpectedly contrasted, considering the above description of the sample: Despite its similar appearance and color, the fossil is enriched in carbon, and no contrast is observed between the vitreous material, the beige patches, and the rest of the fossil (Fig. 1, C and D). The carbon distribution can be used to pinpoint interesting areas for spectroscopy. We collected five full XRS-based carbon K-edge XANES spectra (Fig. 1E), one from the shale and four from the plant, targeting at the different materials observed (at the edge and inside of the diamond-shaped leaf scars) and at the different carbon amounts revealed by the map. The black shale matrix does not contain notable amounts of organic carbon. Unexpectedly again, all four spectra from the fossil appear very similar after background-corrected normalization. The spectra reveal two main absorption features at 285.4 and 293.0 eV attributed to 1s-π* and 1s-σ* electronic transitions in aromatic and olefinic C═C carbons, respectively (*23*). In contrast to the usual low-energy carbon K-edge XANES spectroscopy, bulk probing of the expected random-oriented polycrystalline material allows comparing the intensity of these spectroscopic features.

With a (1s-π*)/(1s-σ*) ratio [that is, 1s-π*/(1s-σ* + arctangent), where the arctangent function models the edge jump in the carbon K-edge XANES spectra] of 0.45, these spectra reveal that the graphitic macromolecular organic carbon composing the *Lepidendron* trunk is not highly ordered but rather similar to bituminous coals (*24*). In contrast to lignite, the spectra of the *Lepidodendron* trunk do not exhibit any clear absorption feature at 288.7 eV attributed to carboxylic functional groups (1s-π* transition).

There is only a limited number of characteristic resonances at the carbon K-edge (*20*, *25*), and the spectra at this edge from the *Lepidodendron* trunk are well explained by a combination of two Gaussians centered at the 1s-π* and 1s-σ* energies and of an arctangent-shaped contribution to account for transitions to the continuum (Fig. 2A). To further test the homogeneity of the carbon speciation over a very large sample area, we collected maps at different characteristic energies (270, 280, 285, 288, 293, and 350 eV). The spectral decomposition of the reduced XRS-based XANES spectra obtained for each pixel using the same Gaussians and arctangent, as well as a linear fit of the Compton background, fits very well to the experimental data (Fig. 2C). The decomposition gives a (1s-π*)/(1s-σ*) ratio of 0.58, well comparable to that obtained for the full XRS-based XANES spectrum collected at the same location (0.45).

The Gaussian distributions highlight two classes of pixels, those belonging to the fossil (high contribution) and those from the shale

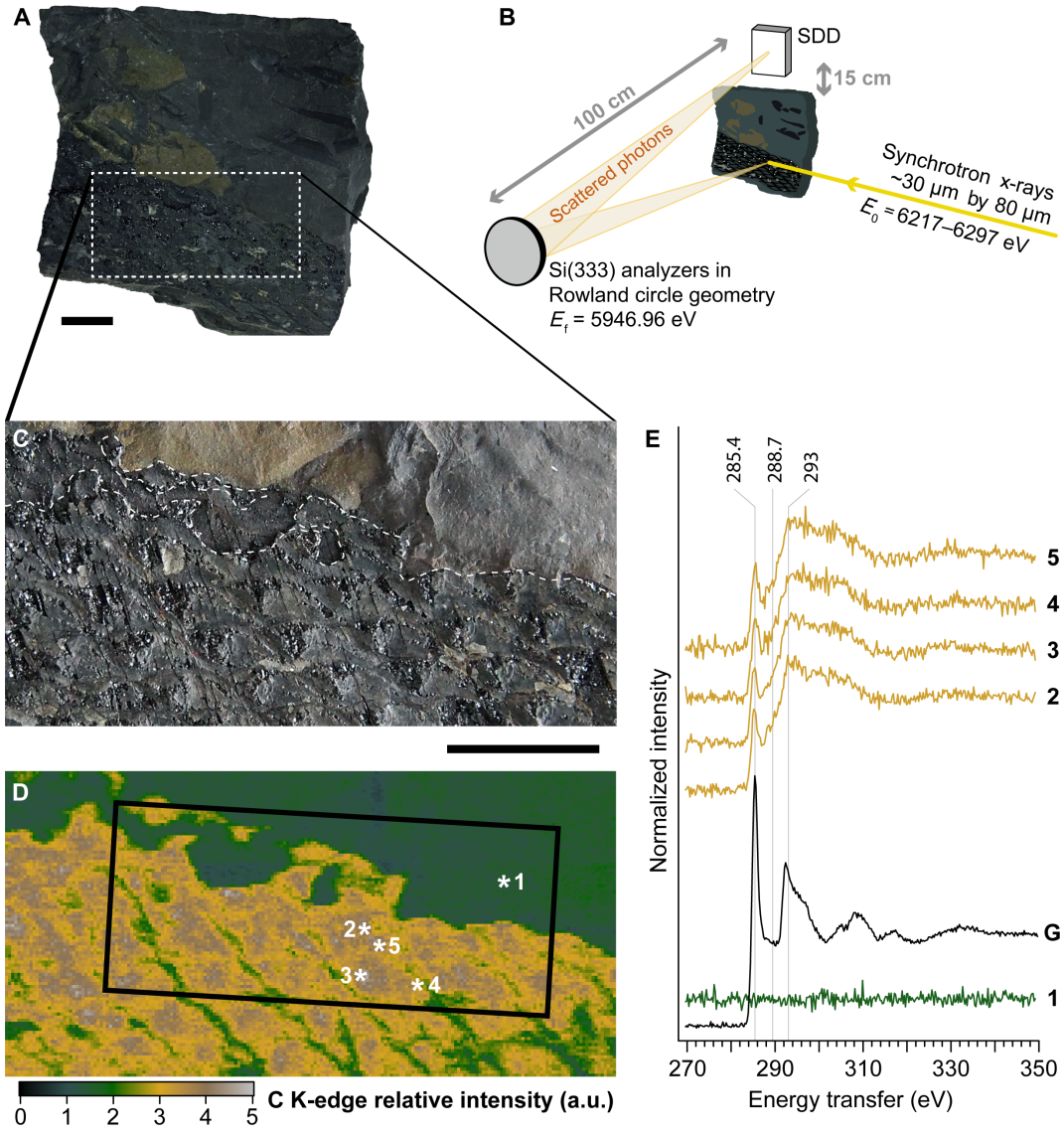

Fig. 1. Carbon XRS mapping and spectroscopy of a fragment of *Lepidodendron* trunk from the Upper Carboniferous (ca. 305 Ma ago) of Noyelles-lez-Lens, France. (**A**) Optical photograph of the studied object. (**B**) Schematic view of the experimental XRS setup. SDD, silicon drift detector. (**C**) Close-up on the studied area. The dashed line represents the boundaries identified in (D). (**D**) Carbon map from the dotted box area in (A) (scan area, 40 mm by 20 mm; 20,000 pixels; scan step, 200 µm by 200 µm; beam size, 15 µm by 15 µm). The box corresponds to the area analyzed in Fig. 2. a.u., arbitrary units. (**E**) Normalized background-corrected carbon K-edge XRS spectra from the locations indicated by asterisks in (D) (sum of four spectra; 500 ms per energy step; beam size, 15 µm by 15 µm), and pure graphite (denoted as "G") for energy calibration and reference; spectra were vertically shifted for an increased readability. Scale bars, 1 cm. (Photo credit: Rafaella Georgiou, CNRS IPANEMA)

matrix (low contribution, reflecting the lower carbon content of the shale; Fig. 1E, spectrum 1). The distribution of the (1s-π*)/(1s-σ*) ratio within the fossil appears quite homogeneous, with a mean ratio of 0.56 (Fig. 2D). This chemical map does not reveal any contrast matching the optical morphology of the sample, as the vitreous material surrounding the diamond-shaped leaf scars remains spectroscopically indistinguishable from the rest of the fossil.

A few pixels yield significantly different ratios: Less than 5 and 2% of the pixels record ratios of <0.35 and >1, respectively, suggesting a complex preservation history with local chemical heterogeneity. Pixels with lower ratios may indicate micrometric "pockets" of preservation, where the plant material has not been turned into coal but only as lignite, or even show the presence of less degraded plant compounds, such as cellulose or lignin, whereas pixels with high ratios indicate the local presence of much more thermally altered compounds.

These results demonstrate the strong potential of 2D XRI to evaluate carbon speciation in heterogeneous fossils. Observation of micrometric "pockets" of preservation appears particularly promising for further molecular identification.

Revisiting the 3D preservation of insect in amber

In dense samples such as rocks, x-rays (6 to 10 keV) penetrate a few tens to hundreds of micrometers. In contrast, they will penetrate from millimeters to centimeters in organic matter. X-rays scattered off the object at different depths along the incident beam direction will focus on different areas of the pixelated detector due to the point-to-point focusing properties of the bent analyzer crystals

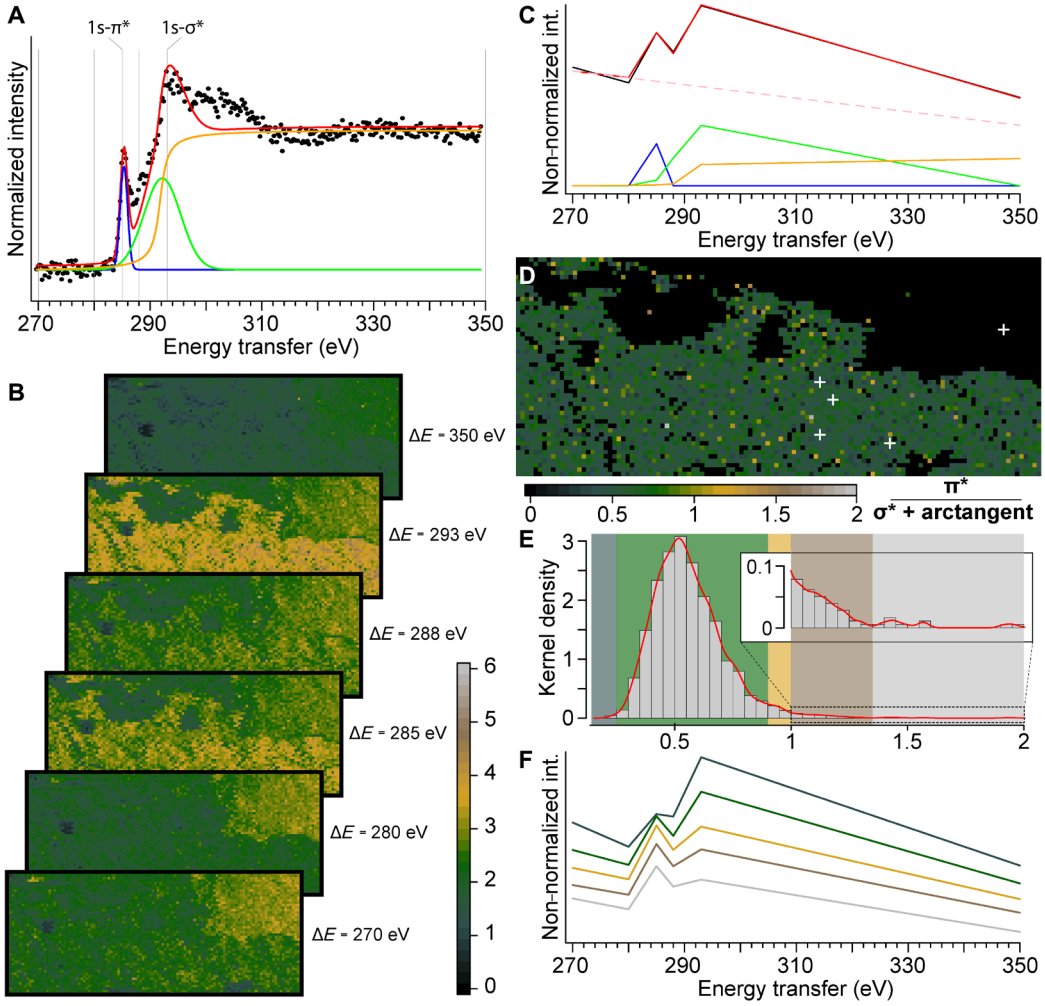

Fig. 2. 2D XRS carbon K-edge speciation mapping of a fragment of *Lepidodendron* trunk from the Upper Carboniferous (ca. 305 Ma ago) of Noyelles-lez-Lens, France. (**A**) Spectral decomposition in two Gaussians and an arctangent of edge features of the normalized background-corrected XRS carbon K-edge XANES spectrum from the location indicated as point "2" in Fig. 1D. (**B**) Carbon intensity maps collected at 270, 280, 285, 288, 293, and 350 eV from the solid box area in Fig. 1D (scan step, 300 μm by 300 μm; 6000 pixels; beam size, 15 μm by 15 μm). Note how accurately the intensities in the fossils match the full spectra collected and how the intensities decrease following the Compton scattering background in the shale. (**C**) Spectral decomposition of the reduced spectrum collected at the exact same location as spectrum point "2" in (A) and Fig. 1D. (**D**) Distribution of the (1s-π*)/(1s-σ* + arctangent) ratio within the *Lepidodendron* trunk (calculated from the spectral decomposition of the reduced spectrum at each pixel). The white crosses indicate the location of the full spectra shown in Fig. 1E. (**E**) Histogram and kernel density of the ratio, allowing to pinpoint a few pixels with a speciation different from the full spectra collected. (**F**) Mean (reduced) spectra from the different classes of ratio identified by their respective colored boxes in (E).

(Fig. 3A). The collection of data along the beam direction thereby provides a 1D image where the contrast is governed by the inelastic scattering signal after proper integration, similar to confocal imaging. The collection of successive sections by raster scanning the object then makes it possible to construct a 3D tomographic volume at a resolution defined laterally by the dimensions of the projected beam and by the detector projected pixel size along the beam [i.e., direct tomography (*19*, *26*)].

We performed 3D XRI of a block of Eocene amber containing a morphologically well preserved ant worker, without wings [Oise, France (ca. 53 Ma old); Fig. 3B]. Experimental conditions were selected to yield a voxel size of 50 × 50 × 50 μm^3, each voxel being associated to its own XRS-based XANES spectrum.

The image of the total signal intensity leads to direct observation of most of the morphology of the fossil (Figs. 3C and 4A). The three tagmata are visible (head, mesosoma, and metasoma including the petiole without showing segment details—the mandibles, maxillary palps, and remnants of three legs), confirming that the hyperspectral dataset contains enough information to contrast different parts of the fossils. A mean spectrum from 150 pixels in the bulk amber (Fig. 4D) exhibits a feature at 285.4 eV attributed to 1s-π* transitions of aromatic-olefinic carbons (a broad feature in the energy range of 287.3 to 289.0 eV) and a feature at 292.4 eV related to C—C 1s-σ* contributions (*23*). Ambers are formed during the polymerization of non-volatile terpenoids, which are the major components of the resins produced as a protective metabolism by many angiosperms and gymnosperms while the volatile terpenoids escape to the atmosphere. The Eocene Oise amber, an Ic-type resin typical of angiosperms derived from Fabaceae sp. (*27*), is characterized by the presence of aromatic-olefinic carbons, attributed to terpenoids, biomarkers of

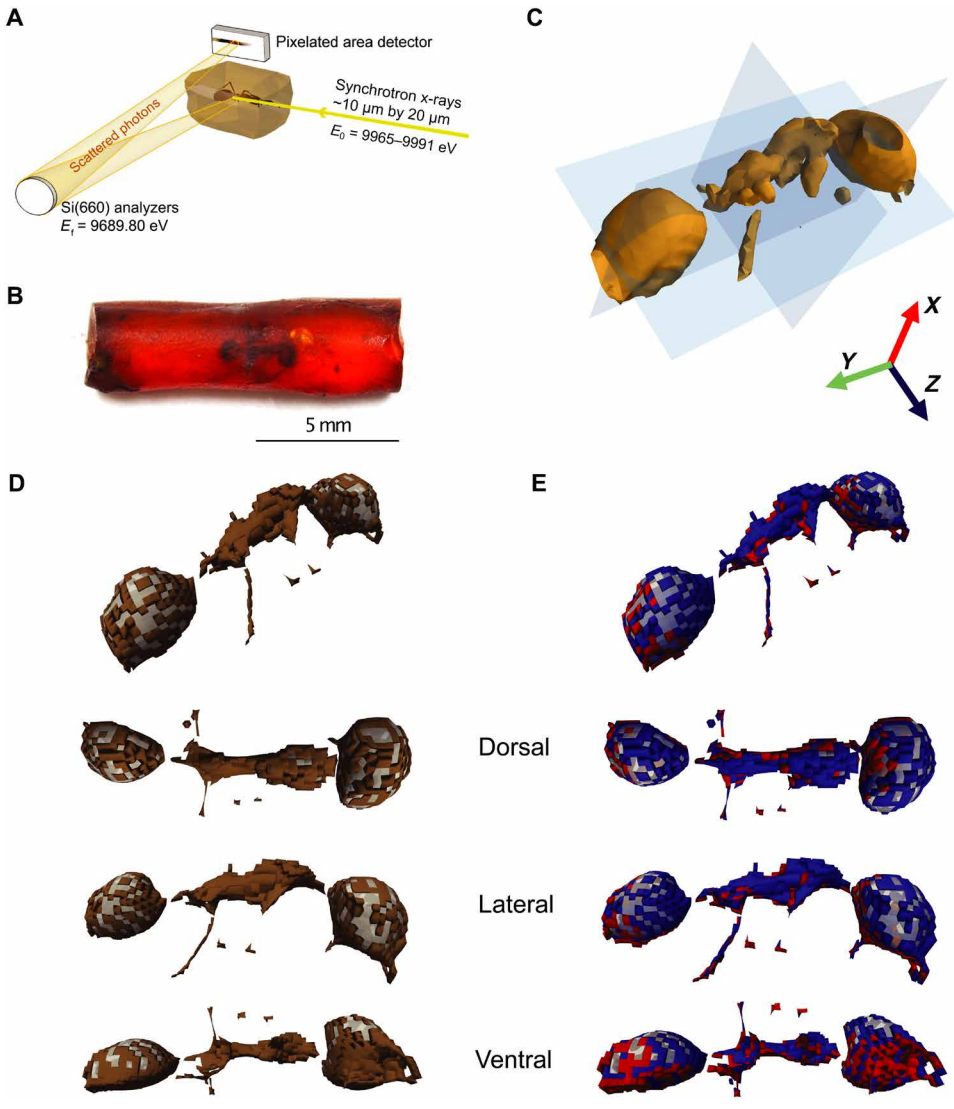

Fig. 3. XRS 3D carbon K-edge speciation mapping of an Eocene (ca. 53 Ma ago) ant entrapped in amber from Oise, France. (**A**) Schematic view of the experimental XRS setup. (**B**) Optical photograph of the specimen. (**C**) Isosurface of the raw, energy-integrated, intensity data. (**D**) 3D rendering of the ant cuticle (brown) and internal void (transparent gray) classes of voxels based on the total signal intensity; image with interpolation [voxel size, 50 μm^3; 23.409 voxels (amber voxels not shown); beam size, 10 μm by 20 μm). Oblique, dorsal, lateral right, and ventral views of the 3D rendering after smoothing (averaged voxel-distance interpolation). (**E**) Clustering of the ant cuticle voxels [brown voxels shown in (D)] based on the A_{chit} parameter allows chemically distinguishing two classes of voxels: one in dorsal right position (negative A_{chit} values in blue) and the other in ventral left position (positive A_{chit} values in red), here shown in oblique, dorsal, lateral right, and ventral 3D views (after smoothing). (Photo credit: Rafaella Georgiou, CNRS IPANEMA)

the botanical origin of the resins (*28*). The broad feature likely corresponds to the superimposition of the 1s-σ* electronic transitions of aliphatic carbons (287.3 to 288.0 eV) (*25*), formed during polymerization (*28*), and of the 1s-π* transitions of carbonyl groups.

Contrasts observed in the specimen indicate the presence of different chemical compounds. Spectra from the perimeter of the insect show features markedly different from the bulk amber. The XRS spectrum $I(\Delta E, X)$ at a given voxel of coordinates $X = (x, y, z)$ is a linear combination of the spectra of the different compounds present and a background signal from valence electron background and Compton scattering

$$I(\Delta E, X) = \sum_{n=1}^{N} A_n(X)\, I_n^{\mathrm{ref,norm}}(\Delta E) + C_1(X) + C_2(X)\,\Delta E \qquad (1)$$

where ΔE is the energy transfer with respect to the K-edge of the element under study. When the model is complete (all reference compounds identified), the A_n parameters reflect the quantity of each species n of normalized XRS spectrum $I_n^{\mathrm{ref,norm}}(\Delta E)$ in the voxel probed. In the restricted ΔE range used, the tail of the background in the XRS spectrum is expected to be quasi-affine in energy and is modeled as $C_1(X) + C_2(X)\Delta E$.

The decomposition of the XRS data was performed as described in Material and Methods, using as initial guess the averaged spectrum of amber measured in the bulk amber (Fig. 4D). As shown on the map of the quadratic error of the fit, the spectral data differ considerably from the amber for a 1-pixel-wide line at the location of the insect's former cuticle (Fig. 4B). Spectra from these pixels show notably different characteristics compared to those of the amber

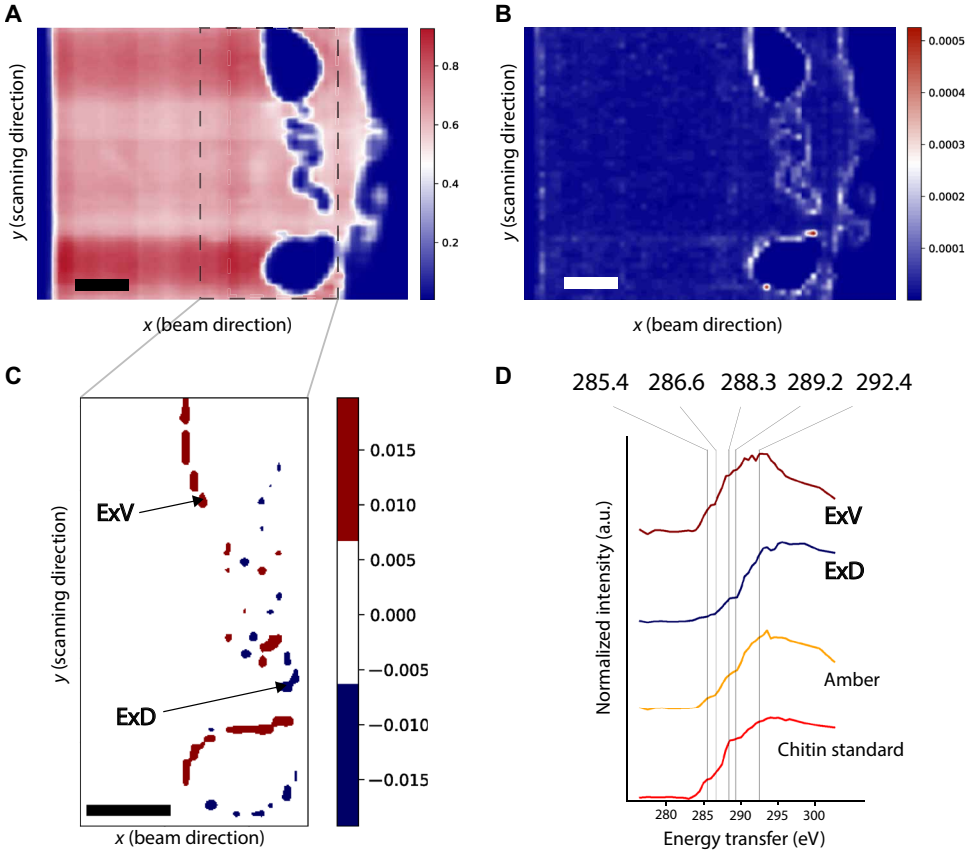

Fig. 4. XRS virtual cross section and spectra of an Eocene ant entrapped in amber from Oise (France, ca. 53 Ma old). (**A**) Total intensity virtual cross-sectional image (pixel size, 50 μm; beam size, 10 μm by 20 μm) of the ant entrapped in the Eocene amber (image with interpolation). (**B**) Spatial distribution of the quadratic error showing the diverse chemical regions of the sample when performing a fit based on the amber reference (image with interpolation). (**C**) Spatial distribution of A_{chit} when performing a fit based on the reference compounds amber and chitin (image with interpolation). (**D**) From top to bottom, distinctive normalized mean XRS spectral profiles corresponding to the ventral (A_{chit} > 0.007, ExV) and the dorsal (A_{chit} < −0.007, ExD) areas of the exoskeleton, as indicated with the arrows in (C), Oise amber collected from the bulk specimen (amber), and chitin standard used as a reference material (chitin standard). Scale bars, 500 μm.

matrix. In particular, some show a more intense feature at 288.3 eV attributed to 1s-π* transitions from amide groups, while others are characterized by the absence of spectral feature at 285.4 eV, which points to the absence of aromatic-olefin carbons.

Arthropods' cuticle is a hierarchically structured material composed of an external thin epicuticle layer, rich in lipids and proteins, and the exocuticle and endocuticle composed mainly of chitin-protein complexes. Chitin [$(C_8H_{13}O_5N)_n$], a linear polymer of β-1,4–linked *N*-acetyl glucosamine, unlike most carbohydrate compounds, is not water soluble and known to be quite decay resistant (*17*, *29*, *30*). We therefore compared the latter spectra to a reference chitin sample measured with XRS spectroscopy under identical conditions. Since both show similar features, we added a chitin reference spectrum to our fitting model. The parameters A_{amb} and A_{chit} predicted from linear least-squares fitting reflect the possible presence of the compounds in each voxel. Positive values of A_{chit} (A_{chit} > 0.007) are observed in the ventral exoskeleton (Fig. 4C, arrow ExV). In contrast, significantly different values (A_{chit} < −0.007) are observed for pixels denoted by arrow ExD, which leads to a second spectrum when segmented (Fig. 4C). We speculate that the negative A_{chit} values in the least-squares regression indicate the presence of an additional chemical compound not included in the model.

The clustering of the data based on A_{chit} allows discussing the chemistry of the arthropod's cuticle. The spectrum ExV is characterized by the presence of 1s-π* transitions due to the presence of aromatic and/or olefinic carbons (Fig. 4D). Both spectra ExV and those from the chitin reference are dominated by a broad complex feature centered at 288.3 eV, which has been attributed to the presence of carbonyl associated with the amidyl group of the glycosyl ring (*17*). The complex feature centered at 289.2 eV of the XRS spectrum of the chitin standard is attributed to the 1s-3p/σ* transition of O-alkyl (C—OH) moieties (*15*). The feature at 286.6 eV, present in the chitin standard, is assigned to the presence of vinyl ketone moieties, a possible result of radiation-induced changes (*31*). The feature at 285.4 eV, assigned to the presence of 1s-π* transition of olefinic moieties, may be indicative of the specimen chemistry and/or result from the elimination of hydroxyl groups from polysaccharides during irradiation as reported by Cody *et al.* (*31*).

In contrast, 1s-π* transitions are totally absent from the arthropod's cuticle close to the specimen dorsal right surface (Fig. 4, C and D, spectrum ExD). The less intense feature of this spectrum, centered at 288.3 eV, is attributed to the overlapping contribution of 1s-π* transitions in amide groups (*15*) and the possible presence of 1s-σ* transitions of aliphatic groups in the energy region of 287.3 to 288.0 eV (*25*). The presence of aliphatic carbons is consistent with the seminal

work of Stankiewicz *et al.* (*32*), which identifies through invasive means aliphatic geopolymers in amber inclusions' exoskeleton, attributed to burial diagenetic transformation of the original chemistry of the organism. Chitin and lignocellulose could be identified using pyrolysis-GC/MS in subfossil (2 to 20 thousand years old) insect and plant specimens entrapped in resins from Kenya, yet no trace of these macromolecules could be identified in Dominican amber inclusions (>25 Ma); instead, aliphatic polymers and sulfur-containing moieties were identified (*32*). Aliphatic signatures were also identified in fossil arthropods preserved in sediments [e.g., (*30*)]. In all the previous examples mentioned, pyrolysis-GC/MS was used at a semiquantitative level; selective sampling does not ensure that the sampling area is representative of the whole specimen. Here, the identification of two distinct chemical fingerprints in the exoskeleton (dorsal right versus ventral left distributions; Fig. 3E) points to the importance of discriminating the spatial distribution of organic compounds in 3D, at a global scale, to provide complete information about the specimens' biochemistry, physiology, molecular evolution or function, or chemical interactions between the organism and the depositional setting. Inclusions in amber occur in several flow sequences and often form multiple inclusions (i.e., syninclusions). Each flow leads to a preservation mode that depends on several unknown factors including time. Coty *et al.* (*33*) highlighted the need for a 3D approach of taphonomy to constrain paleobiological interpretations. Their computed tomography scan of multiple inclusions in the same sample revealed different levels of preservation depending on the resin layer and on the type of organism.

Although amber and copal (fossil tree resin) preserve three-dimensionally and, in superb detail, numerous organisms (insects, feathers, plants, etc.) as a result of entrapment that rapidly dehydrates the inclusions and protects them from water and microbial decay (*3*), many localities only preserve cuticle or hollow molds (such as the ant we studied herein) or no fossils at all, and the processes that control this range in preservation (nature of the resin producer and of the inclusions, environmental conditions, maturation, and reworking) remain essentially unknown (*34*, *35*).

The clustering of the data based on the total intensity allows the discrimination of the inclusion from the surrounding organic substrate. Further decomposition of the cuticle voxels (Fig. 3D, brown voxels) based on the A_{chit} parameter allows the identification of chitin traces distributed in the cuticle (Fig. 3E, red voxels). This wealth of information allows us to report the first ever fully noninvasive 3D speciation of carbonaceous compounds inside a paleontological specimen (Fig. 3). Cuticle voxels with A_{chit} positive and negative values are represented in red and blue colors, respectively. The lack of carbon signal in the internal part of the abdomen and the head (Fig. 3, D and E, transparent gray voxels) points to the poor preservation state of the internal soft tissue structures, while the voxels with chitin affinities (positive A_{chit} values; Fig. 3E, red voxels) confirm the preservation of the cuticular anatomy in the ventral surface of the insect. Until now, chemical characterization has mainly focused on the amber, and very few studies have investigated the inclusions because of the following challenges (*36*): Spectral features from the inclusions are predicted to be very close in wave number to those of the resin, and because compounds of the resin have largely penetrated the inclusions (*32*), sampling and/or spectroscopy techniques only provide average information, which involves destructive sample preparation, restricting their use for rare specimens. The fact that we were able to detect polysaccharide traces and distinguish the preserved insect's exoskeleton from its encasing amber and hollow parts in 3D with reasonable resolution opens entirely new avenues for the chemical characterization of organisms preserved in amber.

CONCLUSIONS AND IMPLICATIONS

Over the past two decades, XRS spectroscopy has been successfully applied for chemical speciation of light element systems and conditions not suited for a soft x-ray probe. Our results shown here extend this capability to the hyperspectral 2D and 3D imaging of organic-rich paleontological specimens and geological objects. The possibility to work on these samples without any specific preparation and under ambient conditions is the critical advantage of this hard x-ray probe. While other imaging methods, most notably x-ray phase-contrast tomography, provide better spatial resolution and are less restricted in terms of sample size and composition, the XRS method shown here uniquely complements such information by providing unprecedented insights into 3D carbon speciation. Given the small cross section and resulting weak signal strength, XRS-based speciation characterization and imaging pose some restrictions for sample size and composition. For 2D imaging, the main restriction is the presence of heavy elements in the sample, which reduce the scattering volume. As current XRS setups operate in the range of 6 to 10 keV, 3D imaging is furthermore restricted to sample sizes and compositions that permit the penetration at these x-ray energies. Further work will aim at minimizing the source of potential radiation-induced damage (*37*). Several directions can be pursued as follows: using cryogenic and anaerobic conditions for some samples, increasing x-ray energy to reduce the photoelectric cross section while increasing the XRS intensity and penetration length, and defocusing the beam in the vertical direction using the so-called 2D sectioning mode (*19*). In addition to ancient fossils, the development of this approach to the study of organic-rich heterogeneous materials shows promise for numerous fields of research, including geosciences, life sciences, materials sciences, and cultural heritage.

MATERIALS AND METHODS

Paleontological samples

Two paleontological samples were examined as follows: (i) a fragment of *Lepidodendron* trunk collected by one of us (P.G.) on an Upper Carboniferous (ca. 305 Ma ago) coal slag heap in Noyelles-lez-Lens, France, on 15 April 2012; (ii) an insect (inv. no. PA-3822, Hymenoptera: Formicidae) entrapped in amber, an Ic-type resin typical of angiosperms and derived from a Fabaceae. The amber deposit of Oise, found in 1996 at the Quesnoy locality in the Oise River area of Paris Basin in France, has been dated back from the earliest Eocene (approximately 53 million years ago) (*38*). The specimen belongs to the paleontological collections of the Muséum National d'Histoire Naturelle (Paris). For comparison, we collected data on purified powder of chitin from shrimp shells (C9752, CAS: 1398-61-4, Sigma-Aldrich, St. Louis, USA).

X-ray Raman–based spectral imaging

All experiments were performed at the GALAXIES and ID20 beamlines at the SOLEIL and the ESRF (European Synchrotron Radiation Facility) synchrotrons, respectively. The spectrometer at the GALAXIES beamline was equipped with four spherically bent Si(444) analyzer crystals operated at a Bragg angle of 86° (*39*). The ESRF spectrometer is equipped to house 72 spherically bent Si(660) analyzer crystals, 36

of which were used in the forward scattering geometry (median scattering angle, 30°) and 36 in the backscattering geometry (median scattering angle, 122°) (*40*), resulting in average momentum transfers of 2.6 ± 0.6 $Å^{-1}$ and 8.8 ± 0.6 $Å^{-1}$, respectively.

On both beamlines, the incident x-ray beam was monochromatized using a cryogenically cooled Si(111) double-crystal monochromator and focused by Kirkpatrick-Baez mirrors to a spot size (V × H) of approximately 10 μm by 20 μm at ID20 and 15 μm by 15 μm at GALAXIES. The overall energy resolution was 1.2 eV.

XRI was performed on the specimens without any prior sampling. 4D volumes were taken at ID20 by scanning horizontally the x-ray beam across the sample, and parametrically varying the sample in the vertical position and the x-ray beam energy to create energy losses in the vicinity of the carbon K-edge (280 to 310 eV). The used step sizes were 50 μm in the horizontal and vertical directions. The energy step was 1 eV over the pre-edge region (276.4 to 282.4 eV), 0.5 eV over the carbon K-edge region (282.4 to 296.4 eV), and 2 up to 302.4 eV.

This is an early-stage development of the technique, and we have tested several configurations at the beamlines including a survey on radiation damage that can occur. The *Lepidodendron* XRS data were collected by continuously scanning the sample in the beam at fixed energy, thus reducing the exposure time. No visible radiation-induced damage was observed in this sample, which is known to be stable under irradiation. In contrast, amber is known to be a very sensitive material under irradiation. The 3D amber volume presented here was collected in a high-flux mode (10^{13} ph/s), resulting in darkening of the exposed area after a dwell time of 2 min. Nevertheless, the spectra still carry the chemical information of the sample original chemistry, and none of the samples show signal corresponding to a substantially altered material (*20*). Optimization to further reduce the impact of irradiation is beyond the scope of this paper; however, we did carry out tests in a low-flux mode (20 times less) and a higher energy resolution, which shows promise to mitigate radiation damage. Further efficient ways to avoid damage are discussed in the conclusions.

3D reconstruction of the XRI data

All data were analyzed using the XRStools program package (*26*), and 3D volumes were created for each energy loss step as described recently (*41*). Last, data from different analyzer crystals were interpolated onto a common energy loss scale to account for the slightly different elastic line energies of the different analyzer crystals, and data from the 36 low–momentum transfer analyzer crystals were averaged.

Statistical processing of the 3D XRI data

Decomposition of the XRS spectrum $I(\Delta E, X)$ was performed according to Eq. 1, using a nonlinear least-squares fitting procedure implemented in Python. Normalized spectra were used as reference spectra, $I_n^{\mathrm{ref,norm}}(\Delta E)$ (see the main text for description of the references used at each processing step). The goodness of fit was evaluated on the basis of the residual (quadratic) sum of squares, $\mathrm{RSS} = \sum_{i=1}^{n} (I_i^{\mathrm{exp}} - I_i^{\mathrm{predicted}})^2$.

REFERENCES AND NOTES

1. M. Hoss, S. Pääbo, N. K. Vereshchagin, Mammoth DNA sequences. *Nature* **370**, 333–334 (1994).
2. H. N. Poinar, C. Schwarz, J. Qi, B. Shapiro, R. D. MacPhee, B. Buigues, A. Tikhonov, D. H. Huson, L. P. Tomsho, A. Auch, M. Rampp, W. Miller, S. C. Schuster, Metagenomics to Paleogenomics: Large-scale sequencing of mammoth DNA. *Science* **311**, 392–394 (2006).
3. G. O. Poinar Jr., R. Hess, Ultrastructure of 40-million-year-old insect tissue. *Science* **215**, 1241–1242 (1982).
4. R. DeSalle, J. Gatesy, W. Wheeler, D. Grimaldi, DNA sequences from a fossil termite in Oligo-Miocene amber and their phylogenetic implications. *Science* **257**, 1933–1936 (1992).
5. R. J. Cano, H. N. Poinar, N. J. Pieniazek, A. Acra, G. O. Poinar Jr., Amplification and sequencing of DNA from a 120–135-million-year-old weevil. *Nature* **363**, 536–538 (1993).
6. D. Penney, C. Wadsworth, G. Fox, S. L. Kennedy, R. F. Preziosi, T. A. Brown, Absence of ancient DNA in sub-fossil insect inclusions preserved in 'Anthropocene' Colombian copal. *PLOS ONE* **8**, e73150 (2013).
7. J. Vinther, D. E. Briggs, R. O. Prum, V. Saranathan, The colour of fossil feathers. *Biol. Lett.* **4**, 522–525 (2008).
8. J. J. Brocks, G. A. Logan, R. Buick, R. E. Summons, Archean molecular fossils and the early rise of eukaryotes. *Science* **285**, 1033–1036 (1999).
9. G. D. Love, E. Grosjean, C. Stalvies, D. A. Fike, J. P. Grotzinger, A. S. Bradley, A. E. Kelly, M. Bhatia, W. Meredith, C. E. Snape, S. A. Bowring, D. J. Condon, R. E. Summons, Fossil steroids record the appearance of Demospongiae during the Cryogenian period. *Nature* **457**, 718–721 (2009).
10. D. E. Briggs, R. E. Summons, Ancient biomolecules: Their origins, fossilization, and role in revealing the history of life. *Bioessays* **36**, 482–490 (2014).
11. N. P. Edwards, H. E. Barden, B. E. van Dongen, P. L. Manning, P. L. Larson, U. Bergmann, W. I. Sellers, R. A. Wogelius, Infrared mapping resolves soft tissue preservation in 50 million year-old reptile skin. *Proc. Biol. Sci.* **278**, 3209–3218 (2011).
12. D. E. Greenwalt, Y. S. Goreva, S. M. Siljeström, T. Rose, R. E. Harbach, Hemoglobin-derived porphyrins preserved in a Middle Eocene blood-engorged mosquito. *Proc. Natl. Acad. Sci. U.S.A.* **110**, 18496–18500 (2013).
13. J. Lindgren, P. Sjövall, V. Thiel, W. Zheng, S. Ito, K. Wakamatsu, R. Hauff, B. P. Kear, A. Engdahl, C. Alwmark, M. E. Eriksson, M. Jarenmark, S. Sachs, P. E. Ahlberg, F. Marone, T. Kuriyama, O. Gustafsson, P. Malmberg, A. Thomen, I. Rodríguez-Meizoso, P. Uvdal, M. Ojika, M. H. Schweitzer, Soft-tissue evidence for homeothermy and crypsis in a Jurassic ichthyosaur. *Nature* **564**, 359–365 (2018).
14. C. Jacobsen, S. Wirick, G. Flynn, C. Zimba, Soft x-ray spectroscopy from image sequences with sub-100 nm spatial resolution. *J. Microsc.* **197**, 173–184 (2000).
15. D. Solomon, J. Lehmann, J. Kinyangi, B. Liang, K. Heymann, L. Dathe, K. Hanley, S. Wirick, C. Jacobsen, Carbon (1s) NEXAFS spectroscopy of biogeochemically relevant reference organic compounds. *Soil Sci. Soc. Am. J.* **73**, 1817–1830 (2009).
16. S. Bernard, K. Benzerara, O. Beyssac, N. Menguy, F. Guyot, G. E. Brown Jr., B. Goffé, Exceptional preservation of fossil plant spores in high-pressure metamorphic rocks. *Earth Planet. Sci. Lett.* **262**, 257–272 (2007).
17. G. D. Cody, N. S. Gupta, D. E. G. Briggs, A. L. D. Kilcoyne, R. E. Summons, F. Kenig, R. E. Plotnick, A. C. Scott, Molecular signature of chitin-protein complex in Paleozoic arthropods. *Geology* **39**, 255–258 (2011).
18. J. Alleon, S. Bernard, C. Le Guillou, J. Marin-Carbonne, S. Pont, O. Beyssac, K. D. McKeegan, F. Robert, Molecular preservation of 1.88 Ga Gunflint organic microfossils as a function of temperature and mineralogy. *Nat. Commun.* **7**, 11977 (2016).
19. S. Huotari, T. Pylkkänen, R. Verbeni, G. Monaco, K. Hämäläinen, Direct tomography with chemical-bond contrast. *Nat. Mater.* **10**, 489–493 (2011).
20. P. Gueriau, J.-P. Rueff, S. Bernard, J. A. Kaddissy, S. Goler, C. J. Sahle, D. Sokaras, R. A. Wogelius, P. L. Manning, U. Bergmann, L. Bertrand, Noninvasive synchrotron-based x-ray Raman scattering discriminates carbonaceous compounds in ancient and historical materials. *Anal. Chem.* **89**, 10819–10826 (2017).
21. W. Schülke, *Electron Dynamics by Inelastic X-ray Scattering* (Oxford Univ. Press, 2007), vol. 7.
22. U. Bergmann, O. C. Mullins, *Asphaltenes, Heavy Oils, and Petroleomics* (Springer, 2007), pp. 139–155.
23. S. Bernard, O. Beyssac, K. Benzerara, N. Findling, G. Tzvetkov, G. E. Brown Jr., XANES, Raman and XRD study of anthracene-based cokes and saccharose-based chars submitted to high-temperature pyrolysis. *Carbon* **48**, 2506–2516 (2010).
24. K. Heymann, J. Lehmann, D. Solomon, M. W. I. Schmidt, T. Regier, C 1s K-edge near edge x-ray absorption fine structure (NEXAFS) spectroscopy for characterizing functional group chemistry of black carbon. *Org. Geochem.* **42**, 1055–1064 (2011).
25. C. Le Guillou, S. Bernard, F. De la Pena, Y. Le Brech, XANES-based quantification of carbon functional group concentrations. *Anal. Chem.* **90**, 8379–8386 (2018).
26. C. J. Sahle, A. Mirone, J. Niskanen, J. Inkinen, M. Krisch, S. Huotari, Planning, performing and analyzing x-ray Raman scattering experiments. *J. Synchrotron. Radiat.* **22**, 400–409 (2015).
27. J. Jossang, H. Bel-Kassaoui, A. Jossang, M. Seuleiman, A. Nel, Quesnoin, a novel pentacyclic *ent*-diterpene from 55 million years old Oise amber. *J. Org. Chem.* **73**, 412–417 (2008).
28. Y. A. Nohra, V. Perrichot, L. Jeanneau, L. Le Pollès, D. Azar, Chemical characterization and botanical origin of French ambers. *J. Nat. Prod.* **78**, 1284–1293 (2015).

29. B. A. Stankiewicz, D. E. G. Briggs, R. P. Evershed, M. B. Flannery, M. Wuttke, Preservation of chitin in 25-million-year-old fossils. *Science* **276**, 1541–1543 (1997).
30. N. S. Gupta, O. E. Tetlie, D. E. G. Briggs, R. D. Pancost, The fossilization of Eurypterids: A result of molecular transformation. *Palaios* **22**, 439–447 (2007).
31. G. D. Cody, J. Brandes, C. Jacobsen, S. Wirick, Soft x-ray induced chemical modification of polysaccharides in vascular plant cell walls. *J. Electron Spectrosc. Relat. Phenom.* **170**, 57–64 (2009).
32. B. A. Stankiewicz, H. N. Poinar, D. E. G. Briggs, R. P. Evershed, G. O. Poinar Jr., Chemical preservation of plants and insects in natural resins. *Proc. R. Soc. Lond. Ser. B: Biol. Sci.* **265**, 641–647 (1998).
33. D. Coty, C. Aria, R. Garrouste, P. Wils, F. Legendre, A. Nel, The first ant-termite syninclusion in amber with CT-scan analysis of taphonomy. *PLOS ONE* **9**, e104410 (2014).
34. X. Martínez-Delclòs, D. E. G. Briggs, E. Peñalver, Taphonomy of insects in carbonates and amber. *Palaeogeogr. Palaeoclimatol. Palaeoecol.* **203**, 19–64 (2004).
35. V. E. McCoy, C. Soriano, S. E. Gabbott, A review of preservational variation of fossil inclusions in amber of different chemical groups. *Earth Environ. Sci. Trans. R. Soc. Edinb.* **107**, 203–211 (2018).
36. H. G. Edwards, D. W. Farwell, S. E. J. Villar, Raman microspectroscopic studies of amber resins with insect inclusions. *Spectrochim. Acta A Mol. Biomol. Spectrosc.* **68**, 1089–1095 (2007).
37. L. Bertrand, S. Schöeder, D. Anglos, M. B. H. Breese, K. Janssens, M. Moini, A. Simon, Mitigation strategies for radiation damage in the analysis of ancient materials. *Trends Anal. Chem.* **66**, 128–145 (2015).
38. A. Nel, G. de Plöeg, J. Dejax, D. Dutheil, D. de Franceschi, E. Gheerbrant, M. Godinot, S. Hervet, J.-J. Menier, M. Augé, G. Bignot, C. Cavagnetto, S. Duffaud, J. Gaudant, S. Hua, A. Jpssang, F. L. de Broin, J.-P. Pozzi, J.-C. Rage, Un gisement sparnacien exceptionnel à plantes, arthropodes et vertébrés (Éocène basal, MP7) : Le Quesnoy (Oise, France). *Comptes Rendus de l'Académie des Sciences - Series IIA - Earth and Planetary Science* **329**, 65–72 (1999).
39. J. M. Ablett, D. Prieur, D. Céolin, B. Lassalle-Kaiser, B. Lebert, M. Sauvage, T. Moreno, S. Bac, V. Balédent, A. Ovono, M. Morand, F. Gélebart, A. Shukla, J.-P. Rueff, The GALAXIES inelastic hard x-ray scattering end-station at Synchrotron SOLEIL. *J. Synchrotron. Radiat.* **26**, 263–271 (2019).
40. S. Huotari, C. J. Sahle, C. Henriquet, A. Al-Zein, K. Martel, L. Simonelli, R. Verbeni, H. Gonzalez, M.-C. Lagier, C. Ponchut, M. M. Sala, M. Krisch, A large-solid-angle x-ray Raman scattering spectrometer at ID20 of the European Synchrotron Radiation Facility. *J. Synchrotron Radiat.* **24**, 521–530 (2017).
41. C. J. Sahle, A. Mirone, T. Vincent, A. Kallonen, S. Huotari, Improving the spatial and statistical accuracy in x-ray Raman scattering based direct tomography. *J. Synchrotron. Radiat.* **24**, 476–481 (2017).

Acknowledgments: Q. Guériau performed the 3D rendering of the fossil ant. R.Ge. and L.B. thank S. Cohen (IPANEMA) for discussion on the processing of the spectral data and L. Beck (LSCE/LMC14). P.G. thanks the Société Amicale des Géologues Amateurs for the organization of the field excursion to the Carboniferous of Artois that allowed collecting the fossil plant from Noyelles-lez-Lens. The ESRF is acknowledged for providing synchrotron radiation, and we are thankful to C. Henriquet for technical support. We acknowledge the SOLEIL synchrotron for the provision of beamtime. R.Ga. thanks A. Nél (ISYEB). We thank D. Sokaras (SSRL), R. Wogelius, and P. Manning (University of Manchester, UK) for insightful discussion about this project. **Funding:** L.B. acknowledges support from the Région Île-de-France/DIM Matériaux anciens et patrimoniaux and the European Commission programs IPERION CH (GA. 654028) and E-RIHS PP (GA. 739503). U.B. and L.B. acknowledge support from the France–Stanford Center for Interdisciplinary Studies Program and the LabEx PATRIMA (Agence Nationale de la Recherche, 10-LABX-0094)/ Fondation des Sciences du Patrimoine. **Author contributions:** L.B. and U.B. conceived the original idea. L.B. and J.-P.R. coordinated the research. P.G. selected the carboniferous fossil plant. R.Ga. selected the Eocene Oise amber. R.Ge., R.Ga., and P.G. provided the paleontological interpretation. J.-P.R. and C.J.S. developed the experimental setups at the GALAXIES and ID20 beamlines, respectively. A.M. wrote the software to integrate the data at the ESRF. R.Ge. developed the code to process the 3D XRI data with L.B. C.J.S., S.B., and U.B. contributed toward the interpretation of the XRS spectra. R.Ge., P.G., and L.B. wrote the manuscript and prepared the figures. R.Ge., P.G., C.J.S., S.B., U.B., J.-P.R., and L.B. took part in the experiments. All authors read and approved the final manuscript. **Competing interests:** All authors declare that they have no competing interests. **Data and materials availability:** All data needed to evaluate the conclusions in the paper have been made publicly available in open access through the following DOIs: 10.5281/zenodo.3238621 and 10.5281/zenodo.3238615.

Submitted 23 February 2019
Accepted 25 July 2019
Published 30 August 2019
10.1126/sciadv.aaw5019

Citation: R. Georgiou, P. Gueriau, C. J. Sahle, S. Bernard, A. Mirone, R. Garrouste, U. Bergmann, J.-P. Rueff, L. Bertrand, Carbon speciation in organic fossils using 2D to 3D x-ray Raman multispectral imaging. *Sci. Adv.* **5**, eaaw5019 (2019).

ScienceAdvances

Carbon speciation in organic fossils using 2D to 3D x-ray Raman multispectral imaging

Rafaella Georgiou, Pierre Gueriau, Christoph J. Sahle, Sylvain Bernard, Alessandro Mirone, Romain Garrouste, Uwe Bergmann, Jean-Pascal Rueff and Loïc Bertrand

Sci Adv **5** (8), eaaw5019.
DOI: 10.1126/sciadv.aaw5019